Application of Compressed Sensing in Brain MR Elastography: Proof of Concept

Grant S. Roberts

***Abstract*— MR elastography (MRE) is a medical imaging technique that is particularly useful in quantifying mechanical properties of tissues by producing a stiffness map (elastogram). Recently, MRE has been applied to the brain to assess stiffness changes in various neurological conditions. Subsequently, compressive sensing (CS) is an image processing technique that aims to accurately reconstruct images from undersampled datasets, which can be used to shorten exam times or improve image quality. This paper aims to assess the feasibility of applying CS towards brain MRE exams. One fully-sampled brain MRE was acquired. K-space data was pseudo-randomly undersampled retrospectively and ℓ^1-wavelet regularized reconstruction was performed. CS reconstructed data were further reconstructed to produce MR elastograms. It was shown using various image quality metrics that undersampling of up to 50% produced accurate MR elastograms.**

I. Introduction

For a number of pathologies, underlying pathological changes result in macroscopic changes in mechanical properties of tissues. This fact has been utilized by physicians for centuries, who have used palpation (examination by touch) as a simple heuristic to aid in diagnosis. A marked example of this is the physical differentiation between soft, benign lipomas and hard, malignant tumors [1]. However, there are other disease processes, such as liver fibrosis, dementia, Parkinson's disease, hydrocephalus, and other disease that cause tissue stiffness changes but cannot be readily palpated. Magnetic resonance elastography (MRE) is a novel MR sequence that produces comprehensive maps of mechanical properties of tissues deep inside the body, termed "virtual palpation", allowing physicians to quantify tissue stiffness without physical palpation [2].

The underlying mechanism behind MRE lies in the motion encoding gradients (MEG's) which are sensitized to the microscopic motion of acoustic shear waves that are introduced into the body by an acoustic driver, operating at a set frequency. The MEG's act to change the phase of spins within slices of interest, as spins that are displaced perpendicular to the direction of shear waves, along the MEG, will acquire some phase. Since shear waves induce only microscopic displacements, MEG's are able to resolve motion on the level of microns, provided the MEG's are well-synchronized the acoustic driver frequency [3]. The phase-encoded displacement information can be measured in image space after applying the Fourier transform to raw k-space data, and shows a still-frame of the shear wave at one point in the shear wave cycle. To produce elastograms, multiple points in the wave cycle must be imaged to provide temporal information (i.e. how the wave propagates through tissues). Thus, multiple images (termed phase-offsets) are acquired for each slice of interest. These phase-offset images are then used to solve for the complex shear modulus of the tissue, directly related to tissue stiffness and elasticity. This is done using complex inversion algorithms, which approximate or analytically solve the wave equation [4].

MRE has recently been applied to the brain, and has shown success in distinguishing between various types of dementia [5]. When imaging other body regions, specifically the liver, respiratory motion becomes a compounding factor, as the MEG's are sensitive to even slight motion. Long breath-holds are often required, placing a large emphasis on fast imaging. Various techniques to reduce scan time have been employed for liver MRE exams, namely undersampling schemes (parallel imaging, partial Fourier acquisitions, etc.). However, because of the lack of respiratory motion artifacts in the brain, breath-holds for brain MRE exams are almost never used. As a consequence, imaging quickly has not been made a large priority and image undersampling is rarely discussed in MRE brain imaging. Despite this, undersampling techniques can still be used towards increasing image quality.

One recently developed image processing theory, termed compressed sensing (CS), allows one to solve ill-posed problems by exploiting image sparsity in some domain [6], [7]. More specifically, if an image is sparse in some transform domain (wavelet, discrete cosine, etc.), random undersampling in Fourier space will appear as incoherent noise once the data is transformed into the sparse domain, at which point the problem becomes a denoising problem. This method has been shown to produce uncompromised images even with drastically undersampled datasets. One study has already shown promise in applying CS to liver MRE exams to reduce scan time [8]. This paper aims to assess the feasibility of applying CS for brain MRE exams by retrospectively undersampling k-space data.

II. Methods

A. Data Acquisition

One healthy volunteer (female, 28 y.o.) was scanned on a GE Signa Premier 3T clinical MR scanner (GE Healthcare, Waukesha, WI). A generic, 2D flow-compensated spin-echo echo-planar imaging (SE-EPI) sequence was implemented, utilizing parallel imaging (ASSET) to accelerate the exam by a factor of 2. Forty-eight slices were acquired from the top of the skull to the inferior aspect of the cerebellum. Further

G. S. Roberts is with the University of Wisconsin - Madison, Madison, WI 53705 USA (corresponding author to provide phone: 816-863-8282; e-mail: gsroberts@wisc.edu).

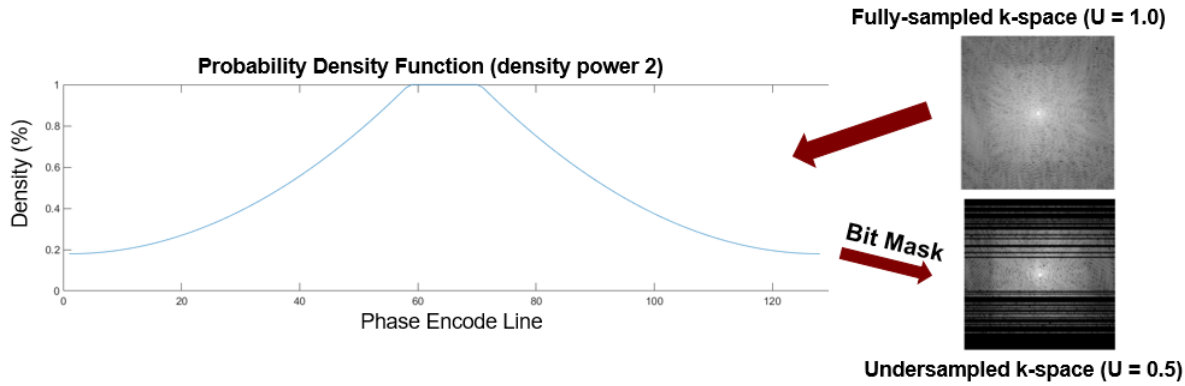

Figure 1. Probability distribution function (PDF) with variable density used to create a 1D pseudo-randomly undersampled bit mask. This bit mask is applied to the fully-sampled dataset to produce retrospectively undersampled k-space in the phase encode direction.

imaging parameters are as follows: TR = 3600 ms; TE = 60 ms; acquisition matrix = 80x80; in-plane resolution = 1.88 mm; slice thickness = 3.0 mm; NEX = 1; phase-offsets = 8; motion encoding sensitivity (MENC) = 6.15 μm/rad; driver frequency = 60 Hz; scan time = 330 s.

After completion of the scan, phase and magnitude images for each phase-offset image set were produced automatically by the scanner, resulting in 16 total images. These images were imported into Matlab (MathWorks, Natick, MA) and were recombined into complex image datasets using (1):

$$\tilde{m}_j(x,y) = M_j(x,y)\exp(i\theta_j(x,y)) \quad (1)$$

where $\theta_i(x,y)$ and $M_i(x,y)$ are the phase and magnitude images respectively (as functions of pixel coordinates *x* and *y*) and the subscript *j* represent the j^{th} phase-offset. The Fourier transform was applied to obtain k-space data, equivalent to the raw data obtained by the scanner.

B. *Retrospective Undersampling*

Raw data were subject to retrospective, pseudo-random undersampling using free Matlab software (SparseMRI, UC-Berkeley). Four datasets containing the original k-space data for each phase-offset were replicated and undersampled with different undersampling factors (U): U = 0 (no undersampling), U = 0.33 (67% of k-space remains), U = 0.50, and U = 0.67, which corresponds to acceleration factors (R) of R =1, R = 1.5, R = 2, and R = 3 respectively. An example of this undersampling scheme is shown in Fig. 1. Undersampling was only performed in the phase-encoding direction, as this is the only feasible way to randomly undersample 2D scans [7]. A variable-density random undersampling bit mask was created from a custom probability density function (PDF). The bit mask for a given undersampling factor was applied to all phase offsets. The PDF acted to ensure pseudo-random undersampling while conserving the desired number of samples. The density power of the PDF was 2 for acceleration factors of 1, 1.5, and 2, and a constraint was added such that the middle 10% of k-space be preserved.

Note that fewer phase-encode lines of k-space directly implies a decreased scan time, as each phase-encode line takes a time TR to acquire. Thus, retrospectively undersampling in the phase-encode direction by a factor U decreases the scan time by the same factor.

C. *Image Analysis*

To analyze image quality, several common metrics were used, namely structural similarity index (SSIM), peak signal-to-noise-ratio (PSNR), and Bland-Altman plots. One of the most commonly used metrics is SSIM, which was used to show relative structural image (perception-based) differences [9]. The full equation for SSIM was derived and is provided in Appendix A. Values for SSIM range from 1 (perfectly similar) to -1 (complete opposite). PSNR (dB) was used to measure the ratio of the maximum possible pixel value in the reference image to the mean square error between the altered images and the reference image. Lastly, Bland-Altman plots were used to measure correlation, bias, and error between identical regions of interest (ROI's) in the same location in the reference image and the reconstructed images. These ROI's were placed over the frontal cortex.

D. *CS Reconstruction*

ℓ^1-wavelet regularized reconstruction was performed on the undersampled datasets for each phase-offset (32 reconstructions in total) using free software (BART Toolbox, UC-Berkeley). The reconstruction is obtained by solving the constrained optimization problem, shown in (2).

$$\begin{aligned} &\text{minimize} \quad \left|\left|Wm\right|\right|_1 \\ &\text{s.t.} \quad \left|\left|F_u m - y\right|\right|_2 < \lambda \end{aligned} \quad (2)$$

where the objective function represents a ℓ^1-norm minimization of the wavelet operator (W) acting on the estimated image vector (m). The constraint function enforces data consistency by constraining the ℓ^2-norm of the difference of the raw k-space (y) and the undersampling Fourier operator (F_u) acting on the estimated image (m) to be less than some regularization parameter (λ).

Optimization of the regularization parameter (λ) was performed for each undersampling factor by repeating the following procedure: (1) Select data from one phase-offset. (2) Perform multiple CS recons with various λ values. (3) Measure SSIM by comparing the non-reconstructed reference image and the reconstructed images at different λ values. (4) Find the lambda associated with maximum SSIM value (λ_{opt}). (5) Repeat this process until accuracy of $\lambda_{opt} < 0.01$. Once the λ_{opt}

was found for each acceleration factor, the CS reconstruction was performed for all phase-offsets at λ_{opt}.

E. MRE Reconstruction

Once the CS reconstructed images were obtained, MRE reconstruction was performed using a free software (MREWave.exe, Mayo Clinic). The software in this algorithm uses local frequency estimation (LFE), a type of inversion technique that approximates stiffness based on local wave speeds calculated from phase offset images. For each acceleration, all 8 CS reconstructed magnitude and phase images were imported into the software. This was also done for the non-reconstructed phase and magnitude images, to produce a reference stiffness map. Initially, the MRE reconstruction was performed on the reference dataset. The brain was segmented and a binary mask from the reference magnitude images and was saved, which would later be applied to the 4 reconstructed datasets. Quality-guided phase unwrapping and high-pass Gaussian filtration (> 4 waves/FOV) was performed on every dataset. The software created stiffness maps for the reference dataset and for the 4 CS reconstructed datasets. In total, 5 MRE reconstructed stiffness maps were produced.

III. Results

Images were successfully obtained for the volunteer and k-space data were successfully reconstructed. Random undersampling masks were successfully created for each acceleration factor and were applied to create retrospectively undersampled k-space. During the CS reconstruction it was found that for acceleration factors of R = 1, 1.5, 2, and 3, the λ_{opt} values were 0.331, 0.004, 0.005, and 0.010 respectively. CS reconstructed images are shown in Fig. 2. While, subjectively, the magnitude images are of good quality, certain regions of the brain (particularly the gyri) in the brain become smoothed with increasing acceleration factors. The phase appears to be more consistent throughout the brain, while noise outside of the brain appears to change drastically between accelerations. Stiffness maps produced from the CS reconstructed images are shown in Fig. 3. The stiffness maps appear highly similar up to an acceleration of R = 2. At R = 3, it is noted that severe image degradation becomes apparent. MRE reconstructed stiffness maps were compared to the reference stiffness map using SSIM and PSNR image analysis, shown in Fig. 4. SSIM measurements decreased steadily from 0.84 to 0.79 until R = 2. SSIM measurements decreased by nearly half from R = 2 to R = 3. This is evidenced by the dissimilarity of R = 3 stiffness map shown in Fig. 3. The PSNR measurements also showed a similar trend.

Figure 3: Stiffness maps for each acceleration factor, shown on identical, Jet color scales.

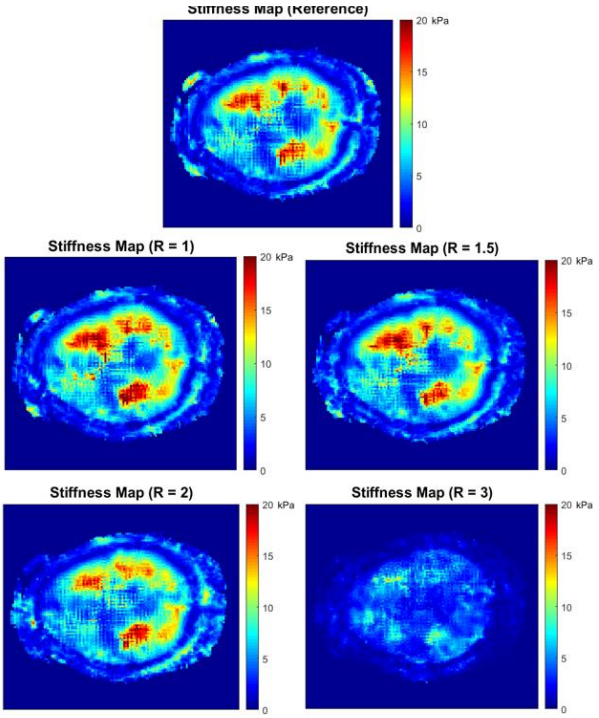

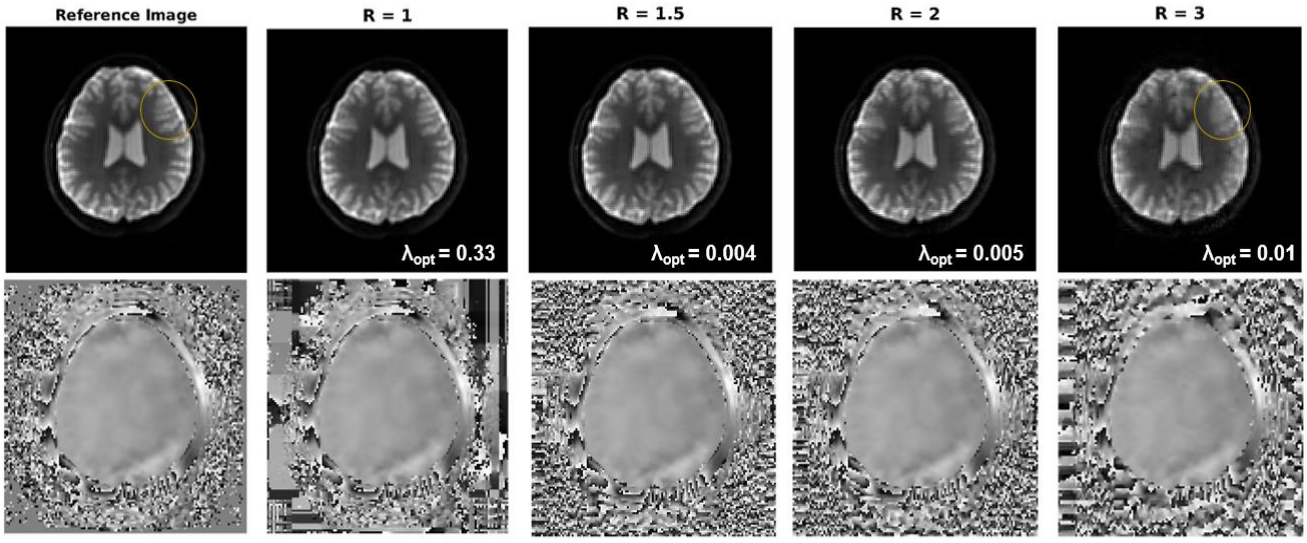

Figure 2. CS reconstructed EPI magnitude and phase images of the brain at increasing undersampling (acceleration) factors are shown for the 1st phase-offset. The orange circle indicates area of the brain that are particularly affected by CS.

Figure 5: PSNR and SSIM image analysis on the MRE reconstructed stiffness maps, CS reconstructed EPI magnitude images, and CS reconstructed EPI phase images for each acceleration factor. The CS reconstructed data was taken from the 1st phase-offset.

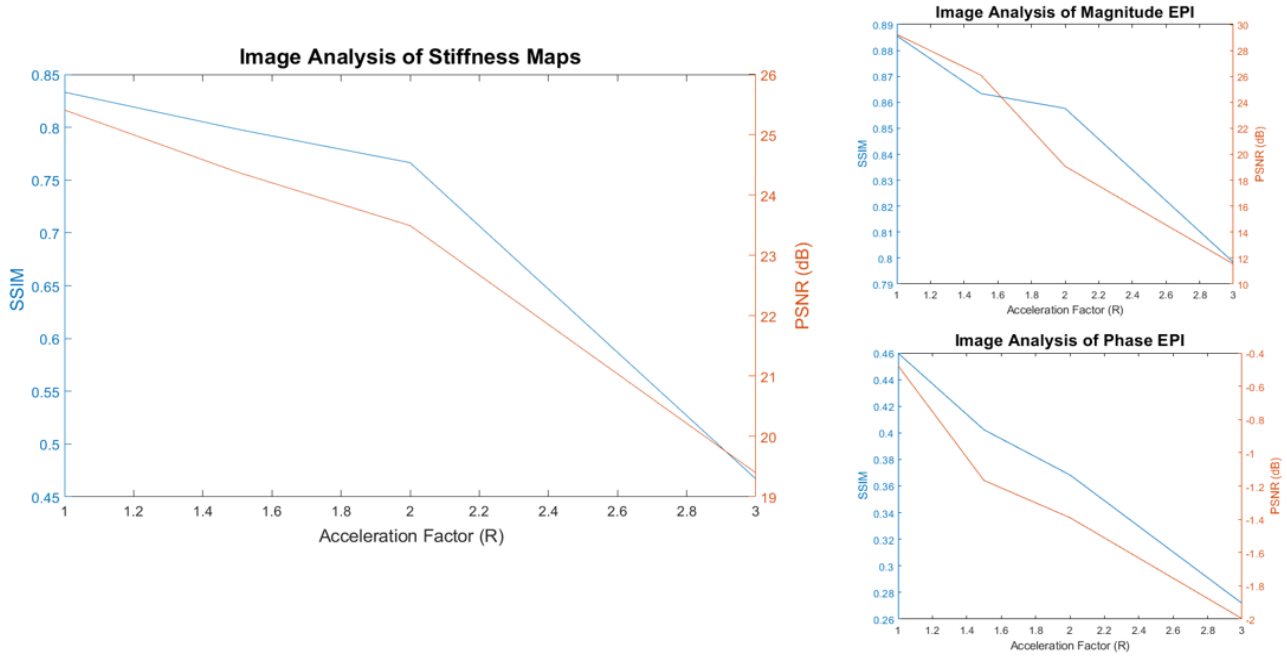

SSIM and PSNR image analysis were also performed on the magnitude and phase EPI images for each acceleration factor (Fig. 4). For both phase and magnitude, SSIM and PSNR decreased approximately linearly. However, the magnitude images showed much higher SSIM and PSNR values compared to the phase images. SSIM in the magnitude images never decreased below 0.8 and PSNR never decreased below 12 dB. Phase images showed much lower SSIM and PSNR values. Even with a non-undersampled, CS reconstructed (R = 1) dataset, SSIM is approximately 0.46 and PSNR is -0.6. Bland-Altman plots also reflect these results. Data within the 20x20 pixel ROI for the reconstructed stiffness maps became less correlated with reference stiffness map ROI data, as seen in Table I. Additionally the magnitude of the ROI bias, 95% confidence interval, and coefficient of variation begin to increase as the acceleration factors increase.

TABLE I. BLAND-ALTMAN ANALYSIS

Accel.	Bland-Altman Analysis Parameters			
	R^2 correlation	***Bias (kPa)***	***95% CI (kPa)***	***Coeff. of Var. (%)***
R = 1.0	0.95	-0.55	3.3	7.1
R = 1.5	0.90	0.03	4.9	11
R = 2.0	0.79	-2.3	7.0	17
R = 3.0	0.38	-6.6	13.7	37

IV. DISCUSSION

From the SSIM, PSNR, and Bland-Altman analyses, it is clear that accelerations of up to 2 produce reliable results. However, an acceleration of 3 produced very low SSIM and PSNR measurements, as well as a clinically unacceptable stiffness bias. These CS accelerations are much lower than are typically seen in other CS articles. This is almost certainly due to the fact that most applications of CS are primarily interested in reconstructing magnitude images and do not incorporate aspects of phase into their image analysis. It is likely that undersampling of k-space adversely impacts both the magnitude and the phase image quality, resulting in less reliable data. The results from this study echo the results obtained in the study where the feasibility of CS in liver MRE was assessed, in which the authors found that an acceleration factors of up to 1.5 to be reliable [8].

One major limitation of this study was restricting the study to only ℓ^1 regularization and one transform domain (wavelet). It is possible that these images are sparse in the temporal (phase-offset) domain, which could be further exploited. Secondly, ℓ^2 regularization was not performed, and it is possible that this may also produce more viable results.

Future directions include testing with different inversion algorithms. Other algorithms, specifically direct inversion, have proven to be more accurate and are much more common on clinical scanners. Testing with these inversion techniques may be more clinically useful and may provide better results. Additionally, 3D acquisitions would allow another dimension of random undersampling, which would help in making the undersampling artifacts more incoherent in the transform domain, and would expectedly increase image quality.

V. CONCLUSION

In conclusion, it appears that compressed sensing is feasible for brain MRE exams. Accelerations of up to 2 produced reliable, high quality images as measured by PSNR, SSIM, and Bland-Altman analyses. Follow-up investigations need to be done regarding different CS reconstruction algorithms.

APPENDIX A

The structural similarity index (SSIM) is the product of luminance (A1), contrast (A2), and structure equations (A3).

$$l(x,y) = \frac{2\mu_x\mu_y + c_1}{\mu_x^2 + \mu_y^2 + c_1} \quad (A1)$$

$$c(x,y) = \frac{2\sigma_x\sigma_y + c_2}{\sigma_x^2 + \sigma_y^2 + c_2} \quad (A2)$$

$$s(x,y) = \frac{\sigma_{xy} + c_3}{\sigma_x\sigma_y + c_3} \quad (A3)$$

where μ_x is the average measurement over some window *x* (size NxN) of an image and μ_y is the average measurement over a different window *y* (also size NxN). σ_x^2 and σ_y^2 define the variance of these windows, and σ_{xy} defines the covariance. c_1 (A4) and c_2 (A5) are two variables to stabilize the division with a weak denominator.

$$c_1 = (k_1 L)^2 \quad (A4)$$

$$c_2 = (k_2 L)^2 \quad (A5)$$

Often, c_3 is defined as $c_2/2$. The SSIM is a weighted combination of the equations above (A6).

$$SSIM(x,y) = l(x,y)^\alpha \times c(x,y)^\beta \times s(x,y)^\gamma \quad (A6)$$

It is common to simply set the exponents (α, β, λ) equal to 1. This results in the commonly known equation below.

$$SSIM(x,y) = \frac{(2\mu_x\mu_y + c_1)(2\sigma_{xy} + c_2)}{(\mu_x^2 + \mu_y^2 + c_1)(\sigma_x^2 + \sigma_y^2 + c_2)} \quad (A7)$$

REFERENCES

[1] Y. K. Mariappan, K. J. Glaser, and R. L. Ehman, "Magnetic resonance elastography: A review," *Clin Anat*, vol. 23, no. 5, pp. 497–511, 2010.

[2] K. P. McGee, "Virtual Palpation: The Role of MR Elastography in Quantifying and Spatially Resolving Tissue Stiffness as a Biomarker of Disease," *J Am Coll Radiol*, vol. 15, no. 5, pp. 778–780, 2018.

[3] S. K. Venkatesh, M. Yin, and R. L. Ehman, "Magnetic Resonance Elastography of Liver: Technique, Analysis, and Clinical Applications," vol. 37, pp. 544–555, 2013.

[4] K. J. Glaser, A. Manduca, and R. L. Ehman, "Review of MR elastography applications and recent developments," *J Magn Reson Imaging*, vol. 36, no. 4, pp. 757–774, 2012.

[5] M. ElSheikh *et al.*, "MR Elastography Demonstrates Unique Regional Brain Stiffness Patterns in Dementias," *AJR Am J Roentgenol*, vol. 209, no. 2, pp. 403–408, 2017.

[6] D. L. Donoho, "Compressed Sensing," *IEEE Trans Inf Theory*, vol. 52, no. 4, pp. 1289–1306, 2009.

[7] M. Lustig, D. Donoho, and J. Pauly, "Sparse MRI: The application of compressed sensing for rapid MR imaging," *Magn Reson Med*, vol. 58, pp. 1182–1195, 2007.

[8] C. E. Morin, J. R. Dillman, S. D. Serai, A. T. Trout, J. A. Tkach, and H. Wang, "Comparison of Standard Breath-Held, Free-Breathing, and Compressed Sensing 2D Gradient-Recalled Echo MR Elastography Techniques for Evaluating Liver Stiffness," *AJR Am J Roentgenol*, vol. 211, no. 6, pp. 1–9, 2018.

[9] Z. Wang, A. C. Bovik, H. R. Sheikh, and E. P. Simoncelli, "Image Quality Assessment: From Error Visibility to Structural Similarity," *IEEE Trans Biomed Eng*, vol. 13, no. 4, pp. 1–14, 2004.